PNAS NEXUS

PNAS Nexus, 2025, **4**, pgaf147
https://doi.org/10.1093/pnasnexus/pgaf147
Advance access publication 7 May 2025
Research Report

Interferon-dependent R-loop induction by Zika virus contributes to growth attenuation

Yijing Zhao[a], Anna D. Metzler[a], Yangping Li[b], Paola Urlich[a], Yilin Wang[b], David M. Gilbert[c], Bing Yao[b] and Hengli Tang[a,*]

[a]Department of Biological Science, Florida State University, Tallahassee, FL 32306, USA
[b]Department of Human Genetics, Emory University School of Medicine, Atlanta, GA 30322, USA
[c]San Diego Biomedical Research Institute, San Diego, CA 92121, USA
*To whom correspondence should be addressed: Email: tang@bio.fsu.edu
Edited By Richard Stanton

Abstract

Zika virus (ZIKV) infection in human neural progenitors triggers DNA damage and activates DNA damage response, leading to cell cycle arrest that can retard brain development. Here, we link the ZIKV-induced S phase arrest to replication fork stalling and R-loop induction. DRIP-seq reveals that ZIKV infection induces R loops at specific loci strongly enriched in the interferon (IFN)-stimulated genes (ISGs). Bromouridine sequencing results further indicate that nascent ISGs transcripts are prone to R-loop induction upon infection. Knockout of IFN receptor eliminated the R loops on ISGs and partially rescued S-phase arrest in infected cells. And overexpression of RNaseH1 reduced ZIKV-mediated DNA damage and cell cycle arrest. We conclude that unscheduled expression of ISGs induced by ZIKV alters R-loop homeostasis and perturbs replication fork progression, leading to fork stalling and eventually DNA damage. IFN-dependent R-loop induction represents a previously unknown, nucleic acid–based mechanism for cell cycle arrest.

Keywords: Zika virus, R loops, interferon, DNA damage response, cell cycle arrest

Significance Statement

Zika virus (ZIKV), a virus that replicates exclusively in the cytoplasm, intriguingly interferes with genome maintenance mechanisms within the host cells. Here, we report that ZIKV infection slows host DNA replication fork progression and triggers R-loop accumulation in interferon (IFN)-stimulated genes, and this mechanism is ZIKV-specific and IFN-dependent. Our results reveal a heretofore unknown function of R-loop dynamics in ZIKV neuropathogenesis and suggest that targeting R loops could be a potential therapeutic strategy against Zika disease.

Introduction

Zika virus (ZIKV) is a mosquito-borne flavivirus in the family Flaviviridae. Since its first isolation in 1947, only sporadic Zika cases had been reported in Africa and Asia until 2007 when an epidemic occurred in Micronesia (1). A larger outbreak occurred in French Polynesia in 2013, from which a suspected link to an increased rate of Guillain–Barré syndrome was reported (2). The more recent 2015–2016 ZIKV outbreak in the Americas saw the virus spread to over 70 different countries and a concurrent increase in microcephaly in babies born to infected mothers. Microcephaly, either present at birth or of postpartum onset, results from the decreased number of neurons and glial cells in the brain due to the imbalance between progenitor cell production and cell death (3). The ability of ZIKV to infect the central nervous system (CNS) of mice was reported by Bell et al. in 1971 (4), and ZIKV was found in the fetal brains of infected pregnant women during the 2015 Brazilian outbreak (5). While the effects of ZIKV infection on multiple cell types in the CNS collectively contribute to ZIKV neuropathogenesis (reviewed in (6)), the ZIKV-induced growth retardation of human neural progenitor cells (hNPCs) (7–12) is an attractive link between infection and impaired early brain development. ZIKV infection of hNPCs induces DNA double-strand breaks and DNA damage response (DDR) (13, 14), leading to an S-phase arrest and growth perturbation.

DNA replication is regulated at the recruitment of the replication machinery to origins and requires extraordinary accuracy (15, 16). However, genomes often face both endogenous and exogenous stressors, which impede the process of DNA replication (17). DNA replication stress is commonly understood as the slowing or stalling of replication fork progression and DNA synthesis, which, while occurring during S phase, can cause broad consequences for mitosis, chromosome segregation, and genomic stability (17, 18). During S phase, a potential collision between transcription and replication machineries makes transcription a major source of replication stress (19). When the nascent RNA strand is inappropriately base

---

Competing Interest: The authors declare no competing interests.
Received: August 20, 2024. **Accepted:** March 31, 2025

paired with the DNA template strand, leaving the nontemplate strand as single-strand DNA, a three-stranded DNA–RNA hybrid structure called an R loop is formed, which can interfere with replication fork progress if not resolved properly (20). Notably, the ataxia-telangiectasia and Rad3-related (ATR) signaling pathway is required to suppress harmful R-loop accumulation by sensing R-loop-impeded replication forks and protects replication forks from excessive MUS81 cleavage (21). The depletion of either ATR or Chk1 induces accumulated R loops and slows down DNA replication progression (22). In addition, many proteins involved in strand elongation and DNA repair have been reported to facilitate R-loop processing and resolution (23, 24).

Here, we report that ZIKV infection slows replication fork progression and triggers co-transcriptionally formed R-loop accumulation. The enriched R-loop sites induced by ZIKV infection are predominantly found in the interferon-stimulated genes (ISGs). This enrichment was not detected in Dengue virus–infected cells or when interferon (IFN) signaling was blocked, demonstrating a ZIKV-specific and IFN-dependent mechanism for the R-loop induction. Additionally, overexpression of human RNase H1, an endonuclease specific for R-loop resolution, suppressed ZIKV-mediated DDR and partially rescued S-phase arrest in ZIKV-infected cells. Our findings highlight the critical role of R-loop dynamics in the cellular response to ZIKV infection and suggest that targeting R loops could be a viable strategy for mitigating ZIKV-induced cellular dysfunction.

Results

ZIKV infection slows down the progression of DNA replication

We previously showed that ZIKV infection of hNPCs and glioblastoma cells induces an S-phase arrest via DNA damage induction (13). To investigate whether DNA replication progression was impacted in ZIKV-infected cells, we performed the DNA fiber assay (25) to directly visualize and quantify the effect of ZIKV infection on replication fork progression. At various time points postinfection, the cells were first labeled with iodo-deoxyuridine (IdU) and then with chloro-deoxyuridine (CldU) for the same amount of time before being subjected to fiber analysis (Fig. 1A). For hNPCs, infection by ZIKV MR766 (ZIKV^{MR}, muliplicity of infection [MOI] 1) eliminated any nucleotide incorporation at times with any appreciable S-phase arrest (Fig. S1A) (7, 13), precluding a quantitative measurement of inhibition of fork progression. The SNB-19 glioblastoma cells produced quantifiable fibers with both labels. We focused on the fibers that represent progressing forks which are ones with green label linked to red label because they had progressed through the first labeling period (the red label) without being stalled by ZIKV up to the start of the green label. On each of these fibers with linked red and green tracks, the ratio of CldU (green) track to IdU (red) track can be used as a measure of replication fork progression. We observed a significantly lower ratio of CldU to IdU lengths in ZIKV-infected cells at 18 and 20 hpi (Fig. 1B). In addition, the total lengths of these double-labeled tracks were shortened in cells infected with ZIKV for 18 and 20 h (Fig. 1B). The percentage of infected cells was comparable at these time points (Fig. S1B). These data indicate that replication fork progression is substantially slowed by ZIKV infection in these human glioblastoma cells.

ZIKV infection induces R-loop formation that is enriched within ISGs

We next investigated whether R-loop formation is altered in ZIKV-infected cells, given their link to DNA replication by quantifying S9.6 antibody-stained R loops in the nucleus (26). We found that, with ZIKV^{MR} infection (MOI 1), 20.85% of the cells contained positive S9.6 signals as bright foci in their nuclei at 18 hpi, whereas only 2.84% of DENV-infected cells (MOI 1) showed the positive S9.6 signal in their nuclei at this time point (Fig. 2A). Importantly, the nuclear staining by the S9.6 antibody was significantly reduced by RNaseH1 treatment, suggesting that the antibody was detecting R-loop structure in the nucleus as expected (27) (Fig. 2A). Next, we performed DRIP-seq (DNA–RNA immunoprecipitation followed by high-throughput DNA sequencing) (28) to profile and compare R-loop sites in mock- or ZIKV-infected SNB-19 cells. Overall, we found more loci with up-regulated R loop in cells infected with either ZIKV^{MR} or ZIKV PRVABC59 (ZIKV^{PR}), consistent with S9.6 nuclear staining (Fig. 2B). Independently, we performed DNA-RNA hybrid immunoprecipitation (DRIP)-qPCR to confirm the R-loop enrichment in a selected group of genes along with positive (constitutive R-loop sites) and negative (sites known to be absent of R loops) controls (28) (Figs. S2A and B). Strikingly, 56 of the 57 genes that contain R loops commonly induced by the two strains of ZIKV are ISGs (Fig. 2C), but not all of these ISGs formed R loops upon treatment with IFN-β (Fig. 2D). Importantly, these ZIKV-induced R-loop loci in most ISGs were not found in the same cells infected with DENV-2 16681 (DENV), suggesting their specific association upon ZIKV infection (Fig. S2D). The R-loop signals were effectively eliminated when the samples were treated with RNaseH1 prior to immunoprecipitation by the S9.6 antibody (Figs. 2D and S2A), again demonstrating the specificity of the DRIP-seq results.

Nascent ISG transcripts are prone to R-loop induction

Because R-loop formation and transcription are tightly linked processes in cells, we applied bromouridine sequencing (Bru-seq) (29) to profile nascent transcripts in mock- or ZIKV-infected cells. Significant overlap was observed between R-loop induction (DRIP-seq) and nascent transcription (Bru-seq) following ZIKV infection (Fig. 3A). Thirty-eight out of the 57 R-loop-enriched genes detected post-ZIKV infection were among the genes undergoing active transcription in infected cells collected at 18 hpi (Fig. 3B). Again, these 38 genes are involved in the antiviral response and almost exclusively ISGs (Figs. 3C and S3A and B). There were 783 genes whose nascent transcripts were commonly up-regulated by both ZIKV^{MR} and ZIKV^{PR}. Among them, 477 genes were ISGs (Fig. 3C, left) (30). In contrast, virtually all genes (37 out of 38) from the Bru-seq up-regulated list that also formed R loops are ISGs (Fig. 3C, right, and D). In addition, for the ZIKV-induced R-loop peaks that localized in up-regulated genes detected by Bru-seq, the log fold change (logFC) of DRIP-seq changes is significantly higher for the ISGs with both strains of ZIKV (Fig. 3E). Together, these data strongly suggest that ISGs are more prone to R-loop formation when they are actively transcribed in response to infection.

ZIKV infection induces IFN signaling–dependent R-loop formation

Next, we performed interferon alpha receptor 1 (IFNAR1) (a subunit of IFN α/β receptor) knockout (IFNAR1^{KO}) experiments to determine whether IFN signaling is required for ZIKV-mediated R-loop induction. We constructed IFNAR1^{KO} cell lines using glioblastoma cells SNB-19 and U-251 MG by CRISPR/Cas9 (Fig. 4A), followed by viral infection and DRIP-seq. The overall R-loop levels as well as the R-loop loci within ISGs were both dramatically decreased in the IFNAR1 KO cells when compared with the wild-type (WT) cells, while the infection rate at 18 hpi remained comparable (Figs. 4B and S4A–C). Importantly, the hallmark of DNA damage

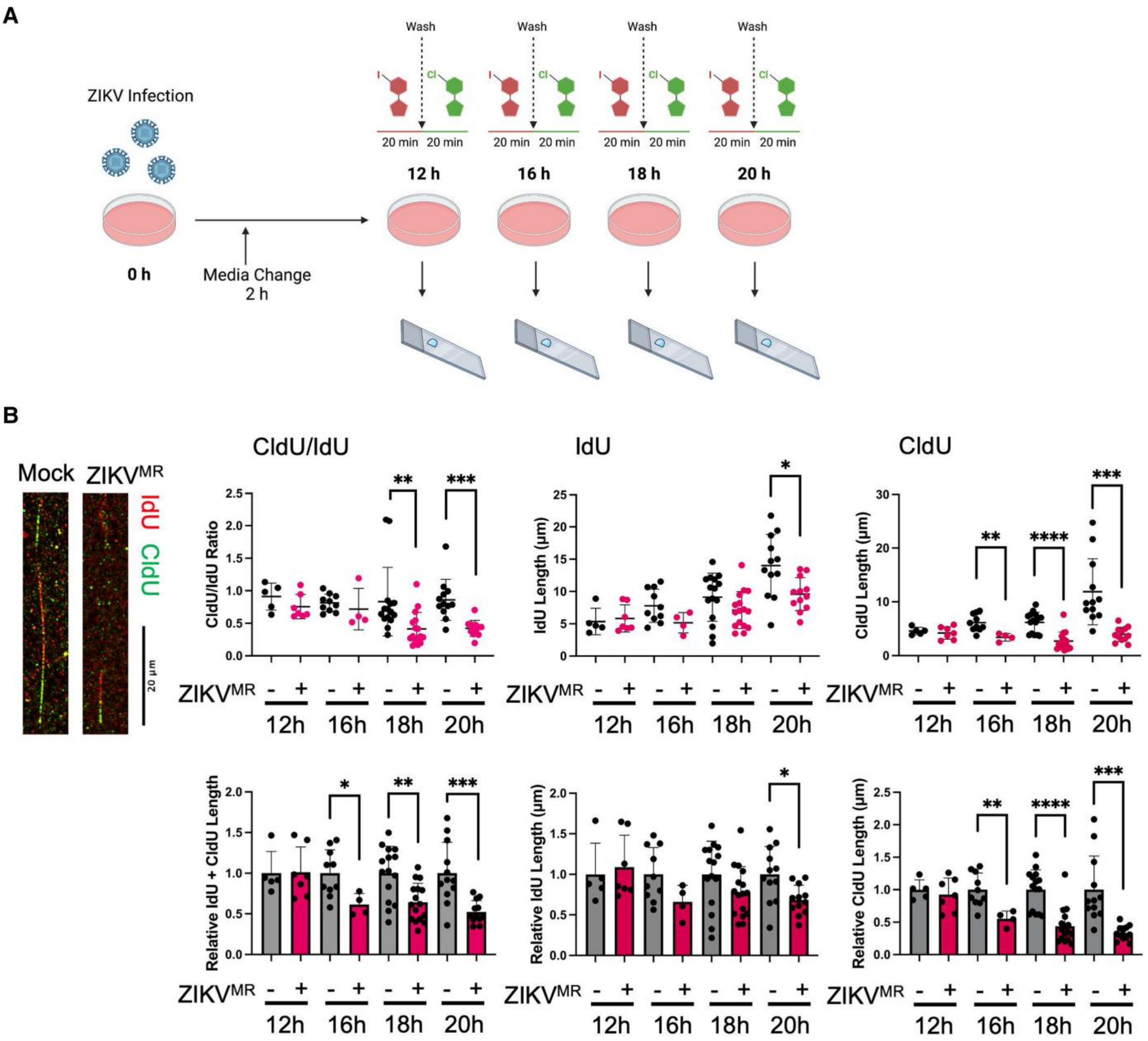

Fig. 1. ZIKV infection slows down the progression of DNA replication. A) Schematic of DNA fiber assay. Prior to thymidine analog labeling, cells were infected with ZIKV^{MR} for 12, 16, 18, and 20 h (MOI 1). At each time point indicated, cells were labeled with 20 μM of IdU for 20 min, followed by a wash and labeling with 200 μM of CldU for 20 min. Samples were then collected for DNA fiber assay. Created with BioRender.com. B) Left: images of DNA fibers in mock- or ZIKV^{MR}-infected SNB-19 cells at 20 hpi (MOI 1). Scale bar is 20 μm. Right top: the ratio of CldU track length to IdU track length of the double-positive fibers in mock- or ZIKV^{MR}-infected cells collected at 12, 16, 18, and 20 hpi. IdU track length and CldU track length of these double-positive fibers. Right bottom: relative total lengths of these double-labeled DNA tracks collected from mock- or ZIKV^{MR}-infected cells. Relative IdU and CldU track lengths of these double-labeled DNA tracks. The lengths were standardized to the average of each mock sample. The error bars are mean ± SD. *$P < 0.05$, **$P < 0.01$, ***$P < 0.001$ (unpaired t test). Source data are provided as a Source Data File.

marker, γH2AX, in ZIKV-infected cells was significantly reduced with IFNAR1^{KO} (Fig. 4C), and the cell cycle profiles of IFNAR1^{KO} cells showed an increased number of cells proceeding to late S phase when infected with ZIKV at MOI 1 (Figs. 4D and S4D). These results demonstrate that IFN signaling contributes to the ZIKV-induced R-loop formation in ISGs, DDR, and the disruption of S-phase progression.

R-loop induction contributes to ZIKV-mediated growth attenuation

RNaseH1 overexpression has been shown to reduce R-loop accumulation (31); so, we determined whether RNaseH1 expression in the human glioblastoma cells was able to alleviate DNA damage or S-phase arrest induced by ZIKV infection. We constructed stable SNB-19 and U-251 MG cells that express either human RNaseH1 or a mutant version without any catalytic activity (32–34) (Fig. S5A). The expression levels of the WT and mutant RNaseH1 in these cells are comparable (Fig. S5B). We then infected these with ZIKV and quantified the number of γH2AX foci in the cells expressing either WT or mutant RNaseH1. We found a statistically significant difference between them, either in the SNB-19 or the U-251 MG cells (Fig. 5A), suggesting that ectopic R loops contribute to ZIKV-induced DDR. We also analyzed the cell cycle profiles using the same comparisons in U-251 MG cells. As shown in Fig. 5B, RNaseH1^{WT} overexpression reduced the effect

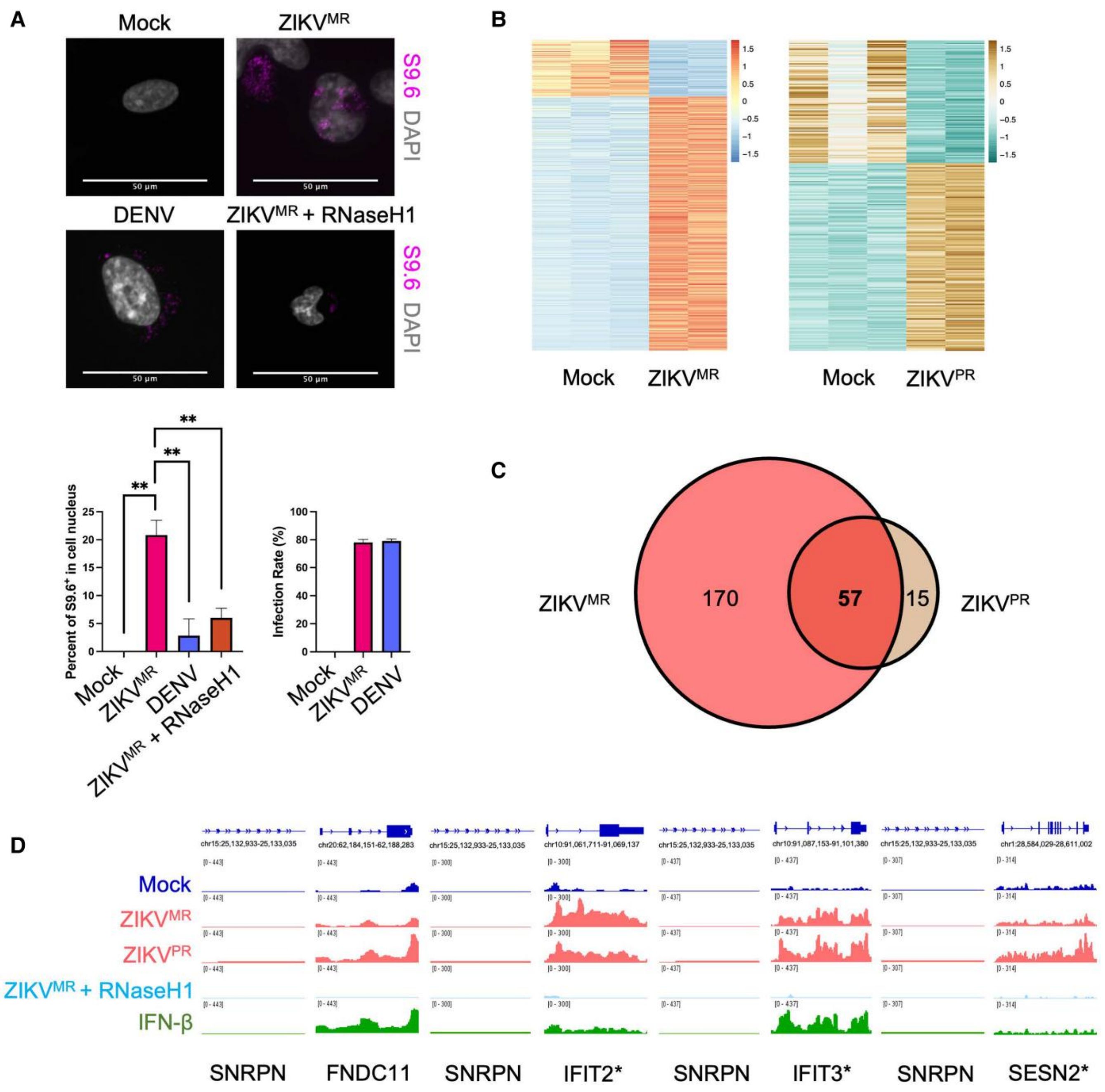

Fig. 2. ZIKV infection triggers R-loop induction in IFN-stimulated genes. A) Top: S9.6 staining of mock- or ZIKV^{MR}- or DENV-infected SNB-19 cells collected at 18 hpi. RNaseH1 was added to the permeabilized cells on the slides before staining in the treatment sample. Bottom left: percentage of cells contained positive S9.6 signals as bright foci in their nuclei after mock or ZIKV^{MR} or DENV infection for 18 h. The error bars are mean ± SD. $n = 2$. Bottom right: the infection rate of mock- or ZIKV^{MR}- or DENV-infected SNB-19 cells (MOI 1). The error bars are mean ± SD. $n = 2$. Scale bars are 50 μm. $^{*}P < 0.05$, $^{**}P < 0.01$, $^{***}P < 0.001$ (one-way ANOVA with Tukey's correction for multiple comparisons). B) Genome-wide significantly up-regulated and down-regulated R-loop regions detected by DRIP-seq in ZIKV^{MR} and ZIKV^{PR}-infected SNB-19 cells (FDR < 0.05). The *y*-axis represents the calculated FC values for each significant locus. C) Venn diagram of the number of common up-regulated genes detected by DRIP-seq in ZIKV^{MR}- or ZIKV^{PR}-infected SNB-19 cells. D) IGV view of DRIP-seq-normalized reads in gene body of FNDC11, IFIT2, IFIT3, and SESN2 of mock- or ZIKV^{MR}-infected SNB-19 cells collected at 18 hpi or IFN-β-treated cells collected at 18 h posttreatment. Results were representative of three experiments for Mock and IFN, and two experiments for ZIKV. RNaseH1 was added to the sample prior to the immunoprecipitation by S9.6 for the treatment sample. ISGs are indicated by an asterisk. Negative control gene is SNRPN.

of ZIKV on S-phase progression to a nonsignificant level, while the S-phase arrest persisted in cells expressing an RNaseH1 mutant. The partial rescue of the cell cycle arrest phenotype by the overexpression of RNaseH1^{WT} supports the notion that unscheduled formation of R loops induced by ZIKV infection contributes to the host cell growth attenuation observed in the ZIKV target cells.

Discussion

The connection between ZIKV infection of human neural cells, especially fast-dividing neural stem cells and glioblastoma cells, and the ensuring cell cycle arrest has been well-established. The phenotype also has significant implications for the unique neuropathogenesis mechanism deployed by ZIKV among flaviviruses to

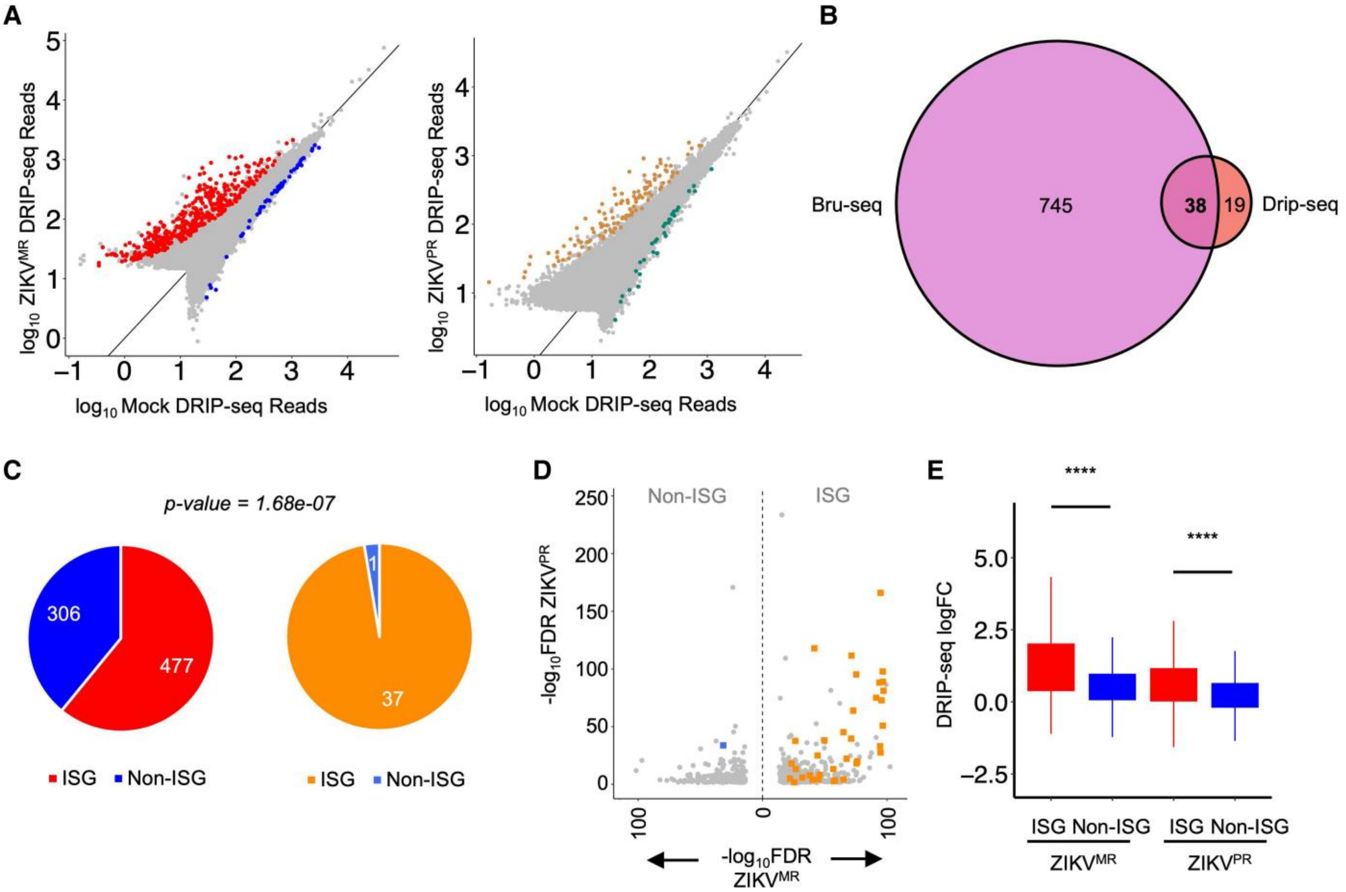

Fig. 3. Nascent ISGs transcripts are prone to R-loop induction. A) Scatter plots that illustrate DRIP-seq reads in R-loop forming regions in Mock- or ZIKV-infected cells. Significant R-loop-accumulated regions with activated transcription in ZIKV^{MR} (left, red) and ZIKV^{PR} (right, gold) are highlighted. Significant R-loop-depleted regions with repressed transcription in ZIKV^{MR} (left, blue) and ZIKV^{PR} (right, green) are also shown. B) Venn diagram showing the overlap of ZIKV-induced R-loop-accumulated genes and genes with activated transcription. C) Pie charts illustrating the number of ISGs and non-ISGs up-regulated by both ZIKV^{MR} and ZIKV^{PR} only in Bru-seq (left) or both in DRIP-seq and Bru-seq (right). P-value was calculated using binomial test. D) The $-\log_{10}$FDR indicating Bru-seq change of ISGs and non-ISGs in ZIKV^{MR}- (x-axis) and ZIKV^{PR}-infected cells (y-axis). Genes with consistent significant DRIP-seq changes are highlighted with either orange (ISGs) or blue (non-ISG). E) DRIP-seq logFC for ISGs and non-ISGs with significantly activated transcription. ****$P < 0.0001$ (unpaired t test).

interfere with brain development. This study fills important gaps within this connection; namely, we found that ZIKV infection leads to nascent ISG transcription, R-loop induction, and DNA replication fork stalling, likely in that order. Along with our previous reports on subsequent steps including DNA damage, DDR, and cell cycle arrest (7, 13), we now provide a complete pathway from unscheduled ISGs transcription and R-loop induction in S-phase cells to a specific S-phase arrest relevant for growth retardation (Fig. 6).

Results from our IFNAR1 KO experiment support a role of IFN signaling in the pathway of R-loop formation in ISGs, DDR induction, and S-phase arrest induced by ZIKV. It has been reported that cytoplasmic accumulation of R loops, as a result of escape from nucleus under manipulated conditions, can trigger IFN production (35), but a function of IFN signaling in the induction of R loops has not been described previously. The remarkable high proportion of ISGs detected in the lists of genes with enriched R loops suggests that unscheduled transcription of ISGs in S-phase cells as a result of ZIKV infection is a potential factor for a conflict between DNA replication and transcription from loci prone to R-loop formation, which is normally not an issue if the genes are not programmed to be expressed under most conditions. Nevertheless, IFN production and signaling do not appear to be sufficient to produce the ZIKV phenotypes. Firstly, DENV infection, which can also activate IFN response, did not trigger R-loop formation in the ISGs; secondly, direct treatment of the SNB-19 cells with IFN-β did not induce the full set of ISG R-loop sites. For example, SESN2, an ISG induced by type II IFN, did not contain increased R loops. And even some of the type I ISGs, such as IFIT2, did not show enriched R loops upon IFN-β treatment. These results are consistent with the functional data that there is a ZIKV-specific component to the mechanisms for both cell cycle arrest in vitro (13, 36) and perturbation of brain development in vivo (6). Interestingly, multiple genes involved in R-loop processing (23, 24) are down-regulated in the Bru-seq sample with ZIKV infection at 18 hpi (Fig. S6), potentially reducing the ability to resolve the ectopic R-loops and exacerbating their negative effect on DNA replication and S-phase progression. The significance and mechanism of the down-regulation remain to be understood. While R-loop formation is typically associated with active transcription, recent studies have shown that R loops can act as inhibitors of transcription by stalling RNA polymerase, and certain R-loop hotspots do not coincide with regions of active transcription, as evidenced in yeast hpr1Δ mutants. The formation of R loops in these mutants can obstruct RNA polymerase II elongation, thereby impairing transcription efficiency (37).

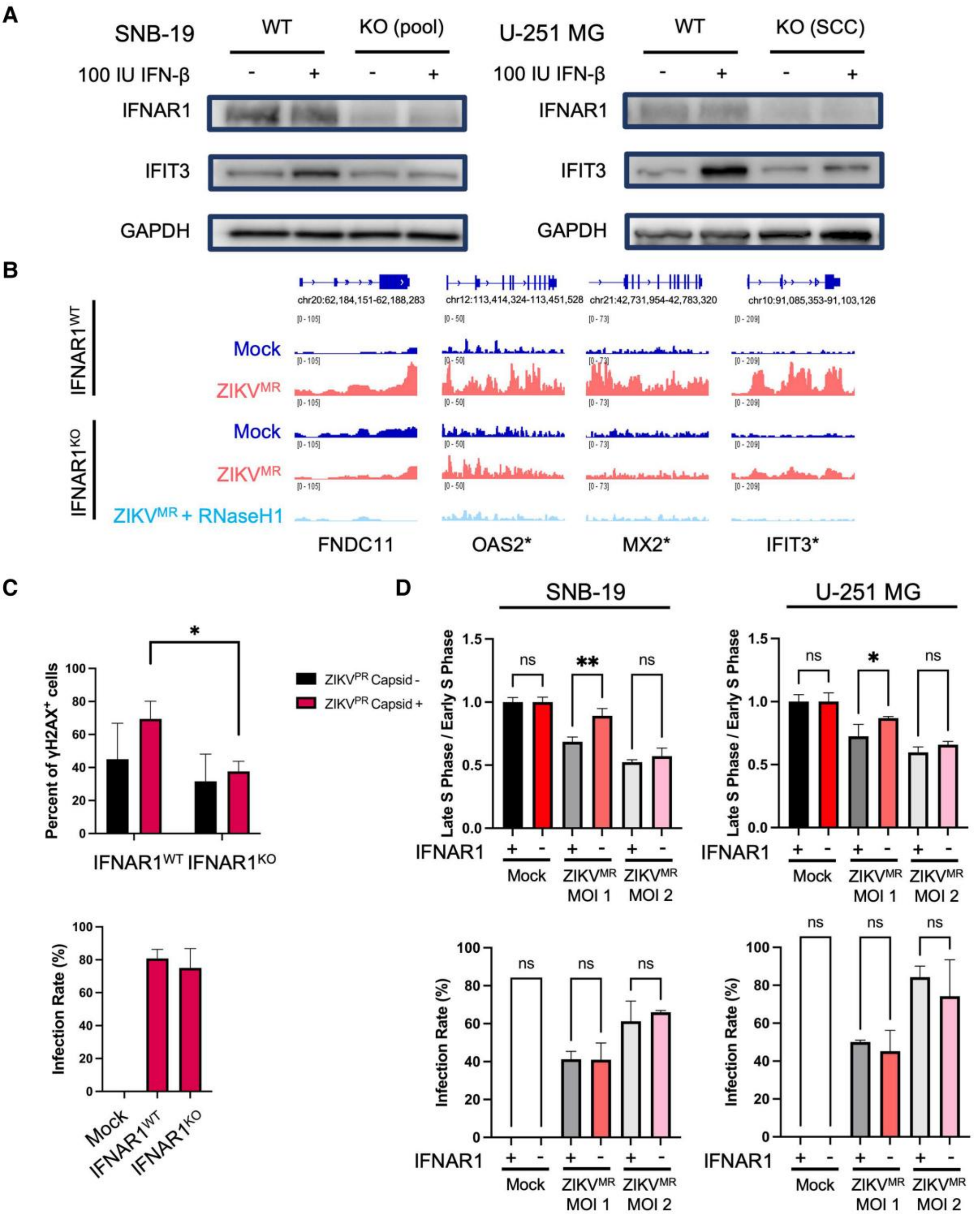

Fig. 4. IFN signaling is critical for ZIKV-induced R-loop enrichment in ISGs. A) Western blot images of IFNAR1$^{\text{WT}}$ and IFNAR1$^{\text{KO}}$ glioblastoma cell lines, showing IFNAR1 and IFIT3 expression upon treatment with 100 IU/mL IFN-β for 12 h. GAPDH was used as loading control. B) IGV view of DRIP-seq-normalized reads in gene body of FNDC11, OAS2, MX2, and IFIT3 of mock- or ZIKV$^{\text{MR}}$-infected U-251 MG/IFNAR1$^{\text{WT}}$ and U-251 MG/IFNAR1$^{\text{KO}}$ collected at 18 hpi (MOI 1). RNaseH1 was added to the sample prior to the immunoprecipitation by S9.6 for the treatment sample. ISGs are indicated by an asterisk. C) Top: percentage of γH2AX^{+} U-251 MG/IFNAR1$^{\text{WT}}$ and U-251 MG/IFNAR1$^{\text{KO}}$ infected with ZIKV$^{\text{PR}}$ collected at 18 hpi (MOI 1). Bottom: the infection rate of mock- or ZIKV$^{\text{PR}}$-infected cells. The error bars are mean ± SD. $n = 2$ or 3. Unpaired t test. D) Top: quantifications of BrdU-pulse-labeled glioblastoma cells analyzed for cell cycle profiles. Late/early S-phase ratios were standardized to the average of each mock-infected cell type. Bottom: the infection rate of mock- or ZIKV$^{\text{MR}}$-infected cells. The error bars are mean ± SD. $n = 3$. Two-way ANOVA with Tukey's correction for multiple comparisons. In both C and D, *$P < 0.05$, **$P < 0.01$.

Although accumulation of unresolved R loops is a likely cause of DNA replication stress and fork stalling, such as in the case of ZIKV infection, programmed formation of R loops participates in important physiological processes. R loops have been shown to facilitate transcription by protecting DNA from DNA methyltransferases and blocking transcription repressors binding at promoters (31, 32). At terminators, R loops aid in transcription termination by promoting RNA polymerase II (RNAPII) pausing

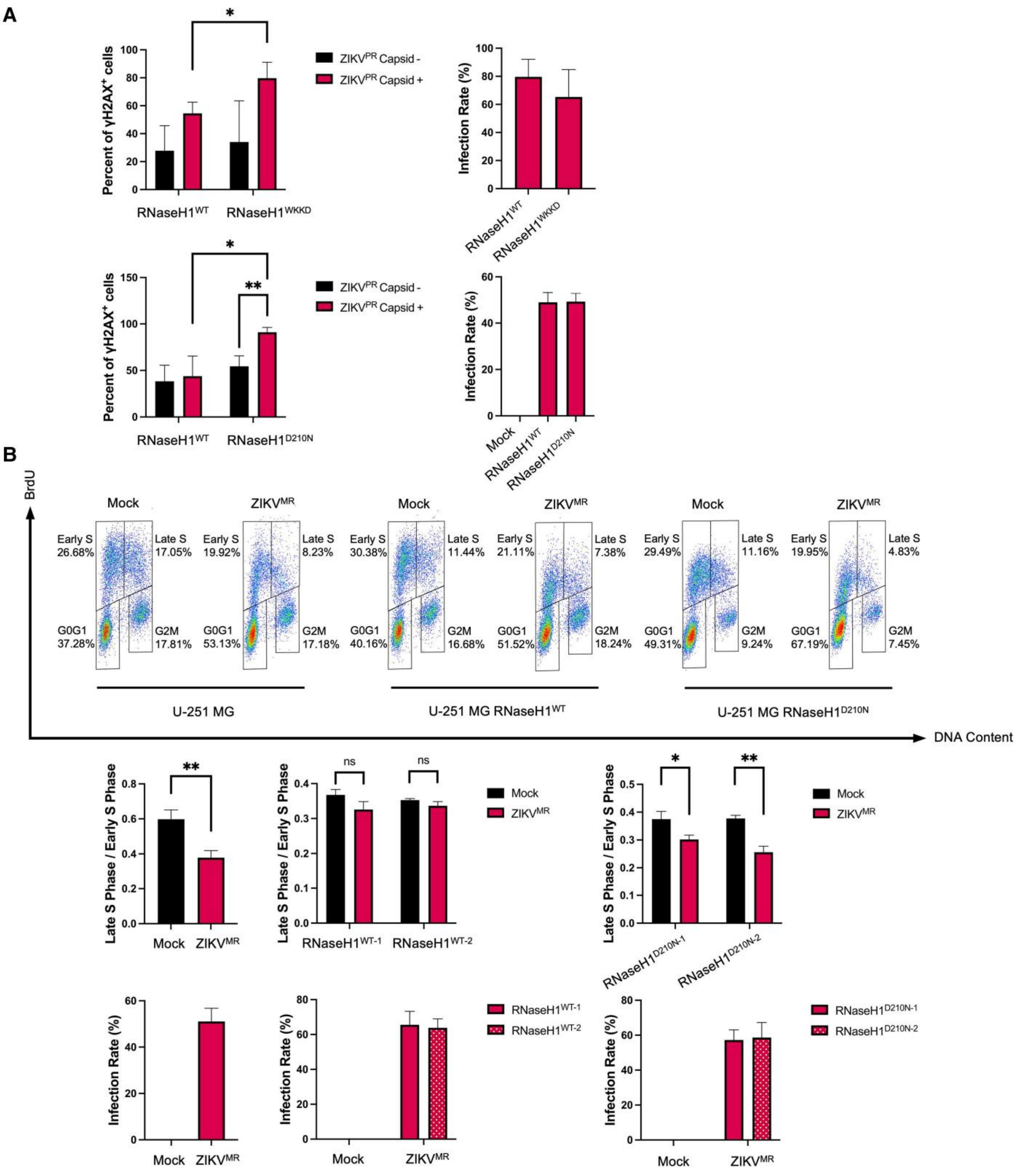

Fig. 5. ZIKV-induced R-loop formation contributes to growth attenuation of infected cells. A) Top: percentage of γH2AX$^+$ SNB-19-RNaseH1^{WT}, SNB-19-RNaseH1^{WKKD} infected with ZIKV^{PR} collected at 18 hpi (MOI 1) and infection rate. Bottom: percentage of γH2AX$^+$ U-251 MG-RNaseH1^{WT}, U-251 MG-RNaseH1^{D210N} infected with ZIKV^{PR} collected at 18 hpi (MOI 1) and infection rate. The error bars are mean ± SD. $n = 2$ (infection rates) or 3 (percentage of γH2AX$^+$ cells). $^*P < 0.05$, $^{**}P < 0.01$ (unpaired t test). B) Top: representative cell cycle profiles of BrdU-pulse-labeled, mock- or ZIKV^{MR}-infected U-251 MGs, U-251 MG-RNaseH1^{WT}, and U-251 MG-RNaseH1^{D210N} collected at 18 hpi (MOI 1). Results were representative images from three independent experiments. Middle: quantifications of late S to early S ratios from the BrdU profiles. The error bars are mean ± SD. $n = 3$. Bottom: the infection rate of mock- or ZIKV^{MR}-infected cells collected at 18 hpi (MOI 1). The error bars are mean ± SD. $n = 3$. $^*P < 0.05$, $^{**}P < 0.01$, $^{***}P < 0.001$ (unpaired t test).

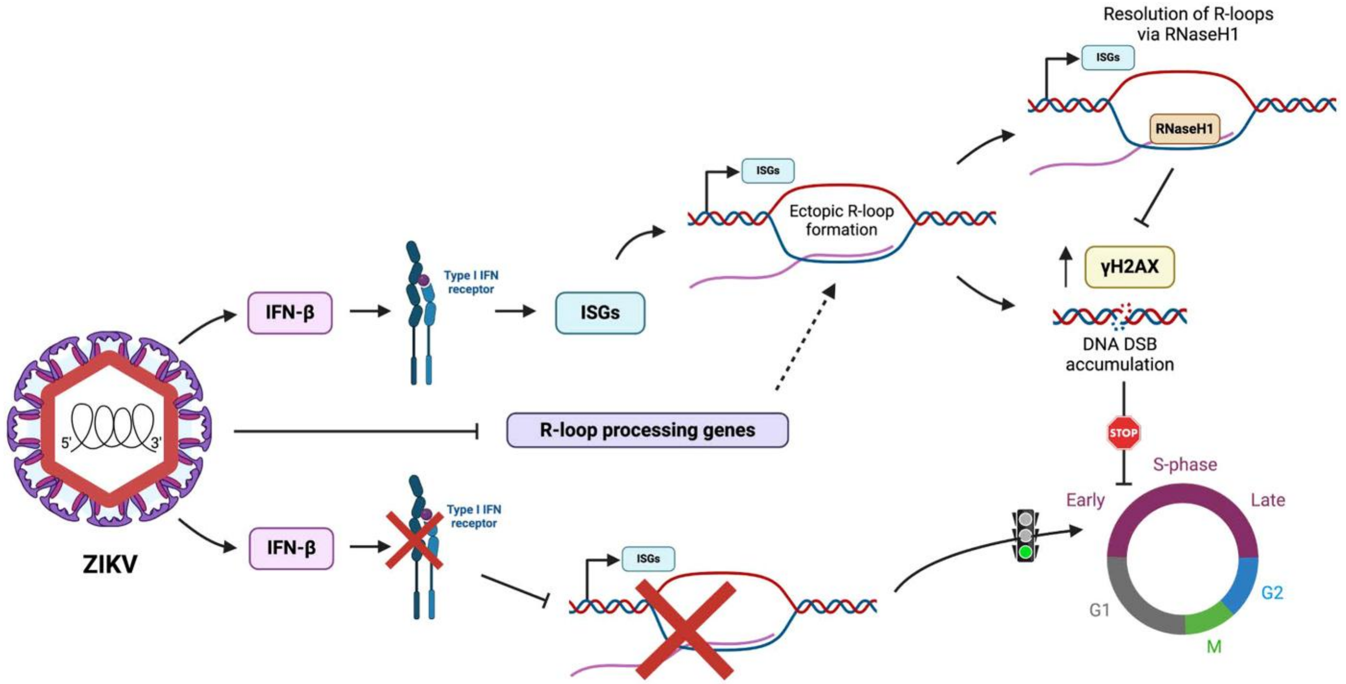

Fig. 6. Proposed mechanism of ZIKV-induced R-loop accumulation. ZIKV infection promotes ectopic R-loop accumulation in ISG gene regions, which is IFN signaling dependent. ZIKV down-regulates R-loop processing genes, which may impair the resolution of R loops, leading to elevated levels of DSBs and ultimately contributing to growth attenuation in infected cells. Created with BioRender.com.

and recruiting R-loop resolution helicases, endonucleases, and RNAi silencing machinery at the transcription end site to cleave and release nascent RNA from its template (31, 33, 38). It has been reported that an increased R-loop level is important for maintaining human papilloma virus (HPV) replication cycle (39). Note that we also found a smaller number of down-regulated R-loop sites in response to ZIKV. The potential effects, if any, of the down-regulated R loops is unclear at this time. Although the effect of RNaseH1 overexpression on ZIKV-induced R loops in these glioblastoma cells has not been directly examined, its impact on cell cycle progression and γH2AX induction indicates that the viral-induced R loops are the likely contributors to the DDR and cell cycle phenotype.

The site-specific enrichment of R-loop loci in ZIKV-infected cells is intriguing. Certainly, the coordinated transcription induction of ISGs upon viral infection likely plays a role in the reproducible pattern that we observed, but the question of why only a subset of ISGs with nascent transcripts were able to have R-loop formation remains as active transcription appears to be necessary but not sufficient for R-loop induction. Experiments that profile DNA damage sites in these cells did not produce any discrete γH2AX-enriched sites or any correlation with the R-loop sites. DNA replication timing analysis also did not reveal any DNA features that indicate a favorable tendency to generate bidirectional replication forks, which increase the possibility of a collision with the transcriptional machinery. However, it remains possible that the relatively higher transcriptional activity in these ISGs alters the local DNA topology by increasing negative superhelicity (40), thereby favoring R-loop-prone regions where their resolution may be less efficient, ultimately leading to their preferential accumulation in this subset of ISGs. Furthermore, how does the local induction of ectopic R loops lead to a global slowdown of DNA replication forks as detected in our fiber assay is puzzling although it has been reported that local toxic DNA lesions can transmit the stress signal to a global response pathway via an ATR-mediated mechanism (41). The two strains of ZIKV that we used in the study differ in passage history and virus lineages, and the higher infection rate of ZIKV^{MR} correlates with its ability to induce more R-loop-enriched sites and higher efficiency of inducing S-phase arrest.

Our study reveals that unscheduled expression of genes, such as ISGs during an infection, can increase the burden of R-loop processing and elevate R-loop formation in the ectopically expressed genes. If not resolved properly, this perturbation of R-loop homeostasis, although initiated locally, can have consequences on global DNA replication progression and cell physiology. These results have broad significance, as induced gene expression under additional stress conditions, such as heat shock or inflammatory response, are common occurrences for cells of higher organisms.

Materials and methods

Cell lines

The SNB-19 cells were cultured in RPMI 1640 medium supplemented with 10% fetal bovine serum (FBS; Gibco, #10437028). The human glioblastoma U-251 MG cells were cultured in Eagle's minimum essential medium (EMEM) supplemented with 10% FBS. Vero cells were cultured in Dulbecco's modified Eagle's medium (DMEM) supplemented with 10% FBS. *Aedes albopictus* C6/36 cells were cultured in EMEM supplemented with 10% FBS and incubated at 28 °C in 5% CO_2. hNPCs were generated in Zhexing Wen's lab (Emory U) following the previous protocols (7, 42).

Virus propagation and infection

C6/36 cells were inoculated with ZIKV or DENV at the indicated MOI for 1 h at room temperature and changed into fresh virus-free medium, followed by incubation at 28 °C in 5% CO_2 for 5–7 days. Supernatant was collected and filtered through a 0.2 μm filter before use or storage. For the focus-forming unit (FFU) assay, a confluent monolayer of vero cells was incubated with serial dilutions of the virus for 2 h at 37 °C, the medium was then replaced with a 2% methylcellulose overlay mixed 1:1 with 2× DMEM, and cells were incubated for 48 to 72 h at 37 °C. Next, 4% paraformaldehyde (PFA) was added to fix cells for 10 min followed by three washes with PBS. The cells were blocked in PBTG (PBT, 0.2% bovine serum albumin [BSA] and 5% normal goat serum) for 30–60 min and incubated with anti-flavivirus envelop 4G2 antibody (1:500 diluted in PBTG) overnight at 4 °C followed by three washes with PBS. The cells were subsequently incubated with goat anti-mouse IgG H&L (horseradish peroxidase [HRP]) secondary antibody (1:500 diluted in PBTG) for 1 h at room temperature, followed by three washes with PBS. The DAB substrate was added to each well, and the plates were shaken on a rotator for 15 min to visualize the foci for the calculation of FFU.

Immunofluorescence staining

For visualizing R loops, cells were seeded on coverslips in 24-well plates before being infected by indicated viruses for 18 h at MOI 1. At 18 hpi, cells were fixed with ice-cold 100% methanol for 10 min on ice, followed by two washes with PBS. Next, cells were blocked in TBST–BSA (TBS, 0.1% Tween-20, and 1% BSA) for 1 h at room temperature and incubated with recombinant anti-DNA:RNA hybrid antibody-S9.6 (Abcam, #ab234957; 1:200 diluted in TBST–BSA) overnight at 4 °C, followed by three washes with PBS. RNaseH1 treatment to cells was done in TBST–BSA supplemented with 3 mM magnesium chloride, and coverslips were incubated with rocking at 37 °C for 1 h, followed by being washed in TBST–BSA for 10 min at room temperature. The cells were subsequently incubated with goat anti-mouse IgG Cy3 secondary antibody (1:500 diluted in TBST–BSA) for 1 h at room temperature, followed by three washes with PBS. The coverslips were mounted using Vectashield mounting medium with DAPI (Vector Laboratories, #H-1200) for confocal imaging.

For infection rates, cells were seeded on coverslips in 24-well plates before being infected by indicated viruses for 18 h at MOI 1. At 18 hpi, cells were fixed with 4% PFA for 10 min, followed by two washes with PBS. Next, cells were blocked in PBTG for 1 h at room temperature and incubated with anti-flavivirus envelop 4G2 antibody (1:500 diluted in PBTG) for 1 h at room temperature, followed by three washes with PBS. The cells were subsequently incubated with goat anti-mouse IgG-FITC (Fluorescein Isothiocyanate) secondary antibody (1:500 diluted in PBTG) or goat anti-mouse IgG Cy3 secondary antibody (1:500 diluted in PBTG) for 1 h at room temperature, followed by three washes with PBS. The coverslips were mounted using Vectashield mounting medium with DAPI for imaging.

For verifying RNaseH1 overexpression single clones, cells were seeded on coverslips and cultured to 70–90% confluency. Cells were fixed with 4% PFA and blocked in PBTG for 1 h. Cells were next stained with the V5-tag (D3H8Q) Rabbit antibody (Cell Signaling Technology, #13202; 1:500 diluted in PBTG). Slides were washed three times with PBS and then stained with goat anti-rabbit IgG-FITC (Sigma Aldrich, #F0382; 1:500 diluted in PBTG). Slides were washed in PBS and mounted using Vectashield mounting medium with DAPI for imaging.

For visualizing γH2AX foci, cells were seeded on coverslips and infected with $\mathrm{ZIKV}^{\mathrm{PR}}$ for 18 h at MOI 1. Cells were fixed with 4% PFA and blocked in PBTG. Cells were stained with the following antibodies: anti-phospho-H2AX (Ser140) (Thermo Fisher Scientific, #MA1-2022; 1:250 diluted in PBTG), anti-ZIKV Capsid (Genetex, #GTX133317; 1:250 diluted in PBTG). Slides were washed three times with PBS and then stained with the following secondary antibodies: goat anti-mouse-Alexa Fluor 647 (1:500 diluted in PBTG) and goat anti-rabbit IgG-FITC (1:500 diluted in PBTG). Slides were washed in PBS and mounted using Vectashield mounting medium with DAPI for imaging. All collected images were analyzed and quantified using ImageJ (https://imagej.net/ij/). The positive phospho-H2AX cells were determined by demonstrating at least one prominent foci with nuclear localization.

BrdU labeling and flow cytometry

Cells were labeled with 100 μM BrdU for 30 min at 37 °C, followed by two washes with ice-cold PBS. Next, cells were trypsinized and resuspended in ice-cold PBS containing 1% FBS. Ice-cold 100% ethanol was added slowly to the cells with gentle shake at a final concentration of 75%. For propidium iodide (PI) staining, cells were denatured by 2 N HCl containing 0.5% Triton X-100 for 30 min, followed by pH neutralization with 0.1 M sodium tetraborate. Next, cells were incubated with 0.15 μg mouse anti-BrdU antibody diluted in wash buffer (PBS, 0.5% Tween-20, and 1% BSA) for 1 h at room temperature, followed by one wash with wash buffer. Cells were then incubated with 1 μg goat anti-mouse FITC diluted in wash buffer for 30 min at room temperature, followed by one wash with wash buffer. Cells were pelleted and resuspended in PI staining buffer and incubated at room temperature for 30 min at room temperature before analysis with a BD FACSCanto machine.

DNA fiber assay

Cells were cultured in 6-well plates for 24 h prior to being infected by ZIKV at MOI 1. Samples were protected from light and prepared as described (25). Cells were incubated with 20 μM IdU for 20 min, followed by two washes with PBS and incubated with 200 μM CldU for 20 min, followed by two washes with PBS. Next, cells were permeabilized with CSK100 buffer (100 mM NaCl, 10 mM MOPS, pH 7, 3 mM $MgCl_2$, 300 mM sucrose, 0.5% Triton X-100) for 10 min at room temperature, followed by careful washing with cold PBS. The exposed nuclei were scraped and pelleted at 7,000 rpm for 5 min at 4 °C to obtain $1–2 \times 10^3$ nuclei/μL. The pellet was resuspended well, and 2 μL of nuclei containing sample was pipetted near the top of the positively charged microscope slides. Eight microliters of LB buffer (200 mM Tris-HCl, pH 7.5, 50 mM ethylene-diamine-tetraacetic acid [EDTA], 0.5% sodium dodecyl sulfate [SDS]) was added to and gently mixed well with the sample to lyse the nuclei for 6–10 min. The slides were then tilted to allow the drop to travel down the slides. After being fixed with freshly prepared methanol mixed 3:1 with acetic acid for 5 min, and denatured in 2.5 M HCl for 1 h, the slides were blocked in 5% BSA in PBS for 30 min at room temperature. The slides were stained with mouse anti-BrdU antibody (1:20 diluted in PBS, 0.05% Tween-20, 1% BSA) and rat anti-BrdU antibody (1:100 diluted in PBS, 0.05% Tween-20, 1% BSA) for 1 h 30 min at room temperature, followed by washes with PBS and PBST. The anti-mouse IgG1 Alexa Fluor 546 and anti-rat Alexa Fluor 488 (1:100 diluted in PBS, 0.05% Tween-20, 1% BSA) were subsequently added to the slides for 1 h at room temperature, followed by washes with PBS and PBST. The slides were mounted using the ProLong Gold Antifade for imaging.

DRIP-seq and DRIP–qPCR

DRIP-seq was performed as described (28). Briefly, cells were cultured in T-75 flasks for 24 h prior to the experiment. For IFN-β treatment, 10 ng/mL of IFN-β was added for 18 h. Cells were collected by trypsinization and pelleting, followed by Dulbecco's phosphate-buffered-saline (DPBS) washes. Cells were resuspended in Tris-EDTA (TE) buffer containing 20% (wt/vol) SDS and 20 mg/mL proteinase K and incubated at 37 °C overnight. On the next day, DNA was extracted and then fragmentated using a cocktail of restriction enzymes at 37 °C overnight. Prior to S9.6 immunoprecipitation, digested DNA was diluted in TE buffer, and 10% of each tube was saved as input for later qPCR. For S9.6 immunoprecipitation, 1× DRIP-binding buffer (10× DRIP-binding buffer: 100 mM sodium phosphate, pH 7, 1.4 M NaCl and 0.5% [vol/vol] Triton X-100) and S9.6 antibody (1 mg/mL) were added to the diluted DNA, followed by incubation at 4 °C on a rotator for 14 to 17 h. Next, DNA from last step was added to the prepared agarose beads and gently rotated at 4 °C for 2 h, followed by two washes with 1× DRIP-binding buffer. DNA was eluted in DRIP elution buffer (50 mM Tris, pH 8, 10 mM EDTA, pH 8, and 0.5% SDS) containing proteinase K, followed by rotation at 55 °C for 45 min. After DNA was purified, the immunoprecipitation efficiency was checked by qPCR. The DNA libraries were constructed for S9.6 antibody immunoprecipitated DNA samples and sequenced on a NovaSeq 6000, with the method of paired-end 150 bp sequencing and 30 M reads. DRIP-seq reads were aligned to the human genome (hg19) by Bowtie 2 version 2.4.4 with default parameters (43). The aligned reads were sorted by genomic coordinates using Samtools (44). Peaks for DRIP-seq were identified by MACS2 version 2.2.6 with their corresponding input BAM file (45). Identified peaks were merged, and reads were re-counted in the merged peak regions. Peaks with a read count exceeding 20 in each replicate of one condition were retained for differential analysis using DESeq2 (46). Significantly, differential peaks were defined by a false discovery rate (FDR) threshold of <0.05. All peaks and differential peaks were annotated to genes using annotatePeaks.pl from HOMER (version 4.11) (47). The R-loop-enriched genes were verified by qPCR.

Bru-seq

Bru-seq was performed as described (29). Briefly, cells were cultured in T-75 flasks for 24 h prior to the experiment. For bromouridine labeling, 6–10 mL of medium of each flask was transferred to clean falcon tubes, and BrU was added to a final concentration of 2 mM. The remaining medium was discarded and BrU containing medium was added back to flasks, and cells were incubated at 37 °C for 30 min. Cells were collected by trypsinization and pelleting. Trizol was then added to the pellet to lyse cells. For total RNA isolation, we added 0.2 mL chloroform per 1 mL Trizol used initially. After dissolving RNA in the nuclease-free water, we applied TURBO DNA-*free* Kit (Invitrogen, #AM1907) to remove any isolated DNA content. The goat anti-mouse IgG magnetic Dynabeads (Invitrogen, #11033) were conjugated with anti-BrdU antibodies (BD Pharmingen, #555627). For isolating BrU-labeled RNA, the total RNA was heated to 80 °C for 10 min and was cooled on ice before being incubated with prepared Dynabeads at room temperature for 1 h. Next, the bead pellet was incubated in nuclease-free water at 95 °C for 10 min to elute BrU-RNA from the beads. The cDNA library was sequenced on a NovaSeq 6000 with the method of single-end 100 bp sequencing and 80 M reads. Bru-seq reads were aligned to the human genome (hg19) by Bowtie 2 version 2.4.4 with default parameters (43). The aligned reads were counted in each gene body of hg19 downloaded from UCSC Table Browser. A gene with a read count exceeding 20 in each replicate of one condition was retained for differential analysis using DESeq2 (46). Significantly differential genes were defined by an FDR threshold of <0.05.

RNaseH1 overexpression cell line construction

Cells were cultured until they were 70 to 90% confluent. Three RNaseH1 plasmids, ppyCAG_RNaseH1_WT, ppyCAG_RNaseH1_D210N, and ppyCAG_RNaseH1_WKKD (Addgene, #111904, #111906, #111905), were prepared in TE buffer. Each of the three RNaseH1 plasmids was mixed well with Opti-MEM medium (Gibco, #31985062) and P3000 solution (Invitrogen, #L3000008) in well-labeled tubes. Lipofectamine 3000 reagent (Invitrogen, #L3000008) was mixed well with Opti-MEM medium in three separate clean tubes. Next, each of the diluted RNaseH1 plasmid solutions was added to each of the diluted Lipofectamine 3000 reagent solutions and incubated for 15 min at room temperature and was then added to cells. Cells were incubated for 2 days prior to antibiotic selection. Next, 600 μg/mL of hygromycin B was added for 2 weeks to select stable RNaseH1 cells. Medium containing hygromycin B was replaced every 2 days.

IFNAR1 CRISPR knockout generation and validation

To generate IFNAR1 KO cells, the sgRNA construct targeting IFNAR1 inserted in a pLentiCRISPRv2 backbone was purchased from GenScript (sgRNA target sequence GATCTAATGTTAAAGACTGG). Lentivirus particles containing the CRISPR/Cas9 system were used for the transduction of glioblastoma cells at a confluency of 30 to 40% to generate IFNAR1-KO cells. After 72 h of transduction, cells were selected with 2 μg/mL puromycin for 2 weeks, followed by single-cell cloning for the U-251 MG KO cells. SNB-19 KO population and U-251 MG KO clones were screened for IFNAR1 expression by western blotting with mouse anti-IFNR1 (ThermoFisher, # MA532006). For the SNB-19 KO cell pool and selected U-251 MG clones, genomic DNA of cells was extracted following the Invitrogen TRIzol Reagent (DNA isolation) user guide (MAN0016385). PCR primers were designed to flank each respective sgRNA target site and amplify the modified region (forward: CAGCTTGCAGCATTCCTGGA and reverse: TGCATCCAGCCCACATAAAGT) for TOPO cloning followed by sequencing (Biosystems 3730 Genetic Analyzer) for cut-site analysis.

Western blotting

Mock- or IFN-β-treated cells were directly lysed in Laemmli sample buffer and immediately boiled for 10 min. Proteins were separated on SDS–8% or 12% polyacrylamide gels and transferred to polyvinylidene difluoride (PVDF) membranes (Millipore) for standard immunoblotting. The primary antibodies used are: anti-IFNAR1 (1:500, ThermoFisher, #MA532006), anti-IFIT3 (1:500, Santa Cruz Biotechnology Inc., #sc-393512), anti-IFITM1/2/3 (Santa Cruz Biotechnology Inc., #sc-374026), or anti-GAPDH (1:20,000, GeneTex, #GTX100118), all diluted in 5% milk in PBST.

Statistical analysis

For DNA fiber assay and quantification of cell numbers, data were analyzed using Excel or Prism software (GraphPad). Data were analyzed using one-way or two-way ANOVA with Tukey's correction for multiple comparisons, two-tailed unpaired t test, or one-tailed exact binominal test, as stated in the legends. Data from repeated independent experiments are presented as the mean ± SD of at least two biological replicates. A *P*-value <0.05 was considered significant. Statistical results can be found in the Source Data file. An FDR threshold of <0.05 was considered significant in identifying significantly differential peaks in DRIP-seq or significantly differential genes in Bru-seq.

Acknowledgments

The authors thank Beth Alexander, Amber Brown, Diego Zorio, Brian Washburn, Cheryl Pye, Cynthia Vied, and Yanming Yang for technical assistance. They thank Sima Jiao, Claire Marchal, Ethan Vouzas, Daniel Bartlett, Yuxiang Li, Yuqing Wang, and Renu Khasa for helpful discussions and technical assistance.

Supplementary Material

Supplementary material is available at *PNAS Nexus* online.

Funding

This project is supported by R01 AI146342 (H.T.) and R01MH117122, R01AG062577, R01AG064786, R01NS118819, and R01AG078937 (B.Y.).

Author Contributions

H.T., B.Y., and Y.Z. conceived and designed the research. Y.Z., A.D.M., and P.U. performed the experiments and collected the data. H.T., D.M.G., B.Y., Y.Z., A.D.M., Y.L., P.U., and Y.W. analyzed and interpretated the data. H.T. and Y.Z. wrote the initial draft of the paper. H.T., D.M.G., B.Y., Y.Z., A.D.M., Y.L., and Y.W. provided the edits. All authors read the manuscript.

Data Availability

The sequencing data have been uploaded to GEO under accession numbers GSE274206, GSE274207, and GSE274208. The secure tokens for reviewer's access are as follows:

GSE274206: ghklkgysxpgljib
GSE274207: azyxaqeentktfyx
GSE274208: khircasgphuxjij

Codes can be accessed at: https://github.com/YaoLabEmory/TangLab.

References

1 Duffy MR, *et al.* 2009. Zika virus outbreak on Yap Island, federated states of Micronesia. *N Engl J Med*. 360:2536–2543.

2 Cao-Lormeau VM, *et al.* 2016. Guillain-Barre syndrome outbreak associated with Zika virus infection in French Polynesia: a case-control study. *Lancet*. 387:1531–1539.

3 Passemard S, Kaindl AM, Verloes A. 2013. Microcephaly. *Handb Clin Neurol*. 111:129–141.

4 Bell TM, Field EJ, Narang HK. 1971. Zika virus infection of the central nervous system of mice. *Arch Gesamte Virusforsch*. 35:183–193.

5 Mlakar J, *et al.* 2016. Zika virus associated with microcephaly. *N Engl J Med*. 374:951–958.

6 Pierson TC, Diamond MS. 2018. The emergence of Zika virus and its new clinical syndromes. *Nature*. 560:573–581.

7 Tang H, *et al.* 2016. Zika virus infects human cortical neural progenitors and attenuates their growth. *Cell Stem Cell*. 18:587–590.

8 Qian X, *et al.* 2016. Brain-region-specific organoids using minibioreactors for modeling ZIKV exposure. *Cell*. 165:1238–1254.

9 Garcez PP, *et al.* 2016. Zika virus impairs growth in human neurospheres and brain organoids. *Science*. 352:816–818.

10 Cugola FR, *et al.* 2016. The Brazilian Zika virus strain causes birth defects in experimental models. *Nature*. 534:267–271.

11 Dang J, *et al.* 2016. Zika virus depletes neural progenitors in human cerebral organoids through activation of the innate immune receptor TLR3. *Cell Stem Cell*. 19:258–265.

12 Li C, *et al.* 2016. Zika virus disrupts neural progenitor development and leads to microcephaly in mice. *Cell Stem Cell*. 19:120–126.

13 Hammack C, *et al.* 2019. Zika virus infection induces DNA damage response in human neural progenitors that enhances viral replication. *J Virol*. 93:e00638-19.

14 Rychlowska M, Agyapong A, Weinfeld M, Schang LM. 2022. Zika virus induces mitotic catastrophe in human neural progenitors by triggering unscheduled mitotic entry in the presence of DNA damage while functionally depleting nuclear PNKP. *J Virol*. 96: e0033322.

15 Alberts B, *et al.* *Molecular biology of the cell*. 4th ed. Garland Science, New York, 2002.

16 Sclafani RA, Holzen TM. 2007. Cell cycle regulation of DNA replication. *Annu Rev Genet*. 41:237–280.

17 Gelot C, Magdalou I, Lopez BS. 2015. Replication stress in mammalian cells and its consequences for mitosis. *Genes (Basel)*. 6:267–298.

18 Zeman MK, Cimprich KA. 2014. Causes and consequences of replication stress. *Nat Cell Biol*. 16:2–9.

19 Crossley MP, Bocek M, Cimprich KA. 2019. R-loops as cellular regulators and genomic threats. *Mol Cell*. 73:398–411.

20 Marnef A, Legube G. 2021. R-loops as Janus-faced modulators of DNA repair. *Nat Cell Biol*. 23:305–313.

21 Matos DA, *et al.* 2020. ATR protects the genome against R loops through a MUS81-triggered feedback loop. *Mol Cell*. 77:514–527.e4.

22 Barroso S, *et al.* 2019. The DNA damage response acts as a safeguard against harmful DNA-RNA hybrids of different origins. *EMBO Rep*. 20:e47250.

23 Brambati A, Zardoni L, Nardini E, Pellicioli A, Liberi G. 2020. The dark side of RNA:DNA hybrids. *Mutat Res Rev Mutat Res*. 784: 108300.

24 Petermann E, Lan L, Zou L. 2022. Sources, resolution and physiological relevance of R-loops and RNA-DNA hybrids. *Nat Rev Mol Cell Biol*. 23:521–540.

25 Quinet A, Carvajal-Maldonado D, Lemacon D, Vindigni A. 2017. DNA fiber analysis: mind the gap! *Methods Enzymol*. 591:55–82.

26 Boguslawski SJ, *et al.* 1986. Characterization of monoclonal antibody to DNA.RNA and its application to immunodetection of hybrids. *J Immunol Methods*. 89:123–130.

27 Bou-Nader C, Bothra A, Garboczi DN, Leppla SH, Zhang J. 2022. Structural basis of R-loop recognition by the S9.6 monoclonal antibody. *Nat Commun*. 13:1641.

28 Sanz LA, Chédin F. 2019. High-resolution, strand-specific R-loop mapping via S9.6-based DNA-RNA immunoprecipitation and high-throughput sequencing. *Nat Protoc*. 14:1734–1755.

29 Paulsen MT, *et al.* 2014. Use of Bru-Seq and BruChase-Seq for genome-wide assessment of the synthesis and stability of RNA. *Methods*. 67:45–54.

30 Rusinova I, *et al.* 2013. Interferome v2.0: an updated database of annotated interferon-regulated genes. *Nucleic Acids Res*. 41: D1040–D1046.

31 Cerritelli SM, Crouch RJ. 1998. Cloning, expression, and mapping of ribonucleases H of human and mouse related to bacterial RNase HI. *Genomics*. 53:300–307.

32 Nowotny M, *et al.* 2007. Structure of human RNase H1 complexed with an RNA/DNA hybrid: insight into HIV reverse transcription. *Mol Cell*. 28:264–276.

33 Nowotny M, *et al.* 2008. Specific recognition of RNA/DNA hybrid and enhancement of human RNase H1 activity by HBD. *EMBO J*. 27:1172–1181.

34 Chen L, *et al.* 2017. R-ChIP using inactive RNase H reveals dynamic coupling of R-loops with transcriptional pausing at gene promoters. *Mol Cell*. 68:745–757.e5.

35 Crossley MP, *et al.* 2023. R-loop-derived cytoplasmic RNA-DNA hybrids activate an immune response. *Nature*. 613:187–194.

36 Liu J, *et al.* 2018. Zika virus envelope protein induces G2/M cell cycle arrest and apoptosis via an intrinsic cell death signaling pathway in neuroendocrine PC12 cells. *Int J Biol Sci*. 14: 1099–1108.

37 Niehrs C, Luke B. 2020. Regulatory R-loops as facilitators of gene expression and genome stability. *Nat Rev Mol Cell Biol*. 21:167–178.

38 Skourti-Stathaki K, Kamieniarz-Gdula K, Proudfoot NJ. 2014. R-loops induce repressive chromatin marks over mammalian gene terminators. *Nature*. 516:436–439.

39 Templeton CW, Laimins LA. 2023. p53-dependent R-loop formation and HPV pathogenesis. *Proc Natl Acad Sci U S A*. 120: e2305907120.

40 Stolz R, *et al.* 2019. Interplay between DNA sequence and negative superhelicity drives R-loop structures. *Proc Natl Acad Sci U S A*. 116:6260–6269.

41 Mutreja K, *et al.* 2018. ATR-mediated global fork slowing and reversal assist fork traverse and prevent chromosomal breakage at DNA interstrand cross-links. *Cell Rep*. 24:2629–2642.e5.

42 Wen Z, *et al.* 2014. Synaptic dysregulation in a human iPS cell model of mental disorders. *Nature*. 515:414–418.

43 Langmead B, Salzberg SL. 2012. Fast gapped-read alignment with Bowtie 2. *Nat Methods*. 9:357–359.

44 Li H, *et al.* 2009. The sequence alignment/map format and SAMtools. *Bioinformatics*. 25:2078–2079.

45 Zhang Y, *et al.* 2008. Model-based analysis of ChIP-Seq (MACS). *Genome Biol*. 9:R137.

46 Love MI, Huber W, Anders S. 2014. Moderated estimation of fold change and dispersion for RNA-seq data with DESeq2. *Genome Biol*. 15:550.

47 Duttke SH, Chang MW, Heinz S, Benner C. 2019. Identification and dynamic quantification of regulatory elements using total RNA. *Genome Res*. 29:1836–1846.